



High-Velocity Impact of Low-Density Projectiles on Structural Aluminum Armor

by B. R. Sorensen, K. D. Kimsey, and B. M. Love

ARL-RP-271

September 2009

A reprint from the *International Journal of Impact Engineering*, Vol. 35, pp. 1808–1815, 2008.

NOTICES

Disclaimers

The findings in this report are not to be construed as an official Department of the Army position unless so designated by other authorized documents.

Citation of manufacturer's or trade names does not constitute an official endorsement or approval of the use thereof.

Destroy this report when it is no longer needed. Do not return it to the originator.

Army Research Laboratory

Aberdeen Proving Ground, MD 21005-5066

ARL-RP-271**September 2009**

High-Velocity Impact of Low-Density Projectiles on Structural Aluminum Armor

B. R. Sorensen, K. D. Kimsey, and B. M. Love
Weapons and Materials Research Directorate, ARL

A reprint from the *International Journal of Impact Engineering*, Vol. 35, pp. 1808–1815, 2008.

REPORT DOCUMENTATION PAGE				Form Approved OMB No. 0704-0188	
Public reporting burden for this collection of information is estimated to average 1 hour per response, including the time for reviewing instructions, searching existing data sources, gathering and maintaining the data needed, and completing and reviewing the collection information. Send comments regarding this burden estimate or any other aspect of this collection of information, including suggestions for reducing the burden, to Department of Defense, Washington Headquarters Services, Directorate for Information Operations and Reports (0704-0188), 1215 Jefferson Davis Highway, Suite 1204, Arlington, VA 22202-4302. Respondents should be aware that notwithstanding any other provision of law, no person shall be subject to any penalty for failing to comply with a collection of information if it does not display a currently valid OMB control number. PLEASE DO NOT RETURN YOUR FORM TO THE ABOVE ADDRESS.					
1. REPORT DATE (DD-MM-YYYY) September 2009		2. REPORT TYPE Reprint		3. DATES COVERED (From - To) 2008	
4. TITLE AND SUBTITLE High-Velocity Impact of Low-Density Projectiles on Structural Aluminum Armor				5a. CONTRACT NUMBER	
				5b. GRANT NUMBER	
				5c. PROGRAM ELEMENT NUMBER	
6. AUTHOR(S) B. R. Sorensen, K. D. Kimsey, and B. M. Love				5d. PROJECT NUMBER	
				5e. TASK NUMBER	
				5f. WORK UNIT NUMBER	
7. PERFORMING ORGANIZATION NAME(S) AND ADDRESS(ES) U.S. Army Research Laboratory ATTN: RDRL-WMT-C Aberdeen Proving Ground, MD 21005-5066				8. PERFORMING ORGANIZATION REPORT NUMBER ARL-RP-271	
9. SPONSORING/MONITORING AGENCY NAME(S) AND ADDRESS(ES)				10. SPONSOR/MONITOR'S ACRONYM(S)	
				11. SPONSOR/MONITOR'S REPORT NUMBER(S)	
12. DISTRIBUTION/AVAILABILITY STATEMENT Approved for public release; distribution is unlimited.					
13. SUPPLEMENTARY NOTES A reprint from the <i>International Journal of Impact Engineering</i> , Vol. 35, pp. 1808–1815, 2008.					
14. ABSTRACT The US Army Research Laboratory has been studying the impact physics of low-density projectiles on urban and light-armor structures for use in electro-magnetic cannons. In this report, results of low-aspect ratio projectiles of nylon, aluminum and steel impacting aluminum armor at velocities above 2000 m/s will be presented. Both computational solid mechanics and analytic modeling techniques were used to supplement experiments to derive a toolkit for assessing target response and character of the debris created from different constant energy impact conditions.					
15. SUBJECT TERMS hypervelocity impact, KE projectiles, low-density projectiles, aluminum armor					
16. SECURITY CLASSIFICATION OF:			17. LIMITATION OF ABSTRACT UU	18. NUMBER OF PAGES 14	19a. NAME OF RESPONSIBLE PERSON B. R. Sorensen
a. REPORT Unclassified	b. ABSTRACT Unclassified	c. THIS PAGE Unclassified			19b. TELEPHONE NUMBER (Include area code) 410-278-6527



Contents lists available at ScienceDirect

International Journal of Impact Engineering

journal homepage: www.elsevier.com/locate/ijimpeng

High-velocity impact of low-density projectiles on structural aluminum armor

B.R. Sorensen*, K.D. Kimsey, B.M. Love

Army Research Laboratory, AMSRD-ARL-WM-TC, APG, MD 21005-6055, United States

ARTICLE INFO

Article history:

Available online 5 August 2008

Keywords:

Hypervelocity impact
KE projectiles
Low-density projectiles
Aluminum armor

ABSTRACT

The US Army Research Laboratory has been studying the impact physics of low-density projectiles on urban and light-armor structures for use in electro-magnetic cannons. In this paper, results of low-aspect ratio projectiles of nylon, aluminum and steel impacting aluminum armor at velocities above 2000 m/s will be presented. Both computational solid mechanics and analytic modeling techniques were used to supplement experiments to derive a toolkit for assessing target response and character of the debris created from different constant energy impact conditions.

Published by Elsevier Ltd.

1. Introduction

In support of the U.S. Army's advanced technology objective in electro-magnetic (EM) gun technology, the Army Research Laboratory has been studying the terminal ballistics of conventional and non-conventional high-velocity kinetic energy projectiles against urban, light-armor and heavy-armor targets. The purpose is to identify and analyze both mechanisms and concepts to effectively defeat a range of targets with inert payloads using the elevated impact velocities available from an EM gun; i.e. for this class of targets, increased diameter, rather than length and density, may be the key to maximize damage in and behind the target. To this end, a series of experiments have been performed launching stubby, low-density projectiles against aluminum armor at velocities above 2000 m/s to observe crater and spall formation and to determine the damage capacity of the debris. In addition, numerical simulations and analytical modeling have been conducted to gain additional insight into the evolution and characteristics of the behind-armor-debris generated from these high-velocity conditions.

The combined experimental, computational, and analytical program reported in this paper examined cylindrical projectiles of nylon 6/6, 6061-T6 aluminum, and 4340 steel and 6061-T6 aluminum conical projectiles striking finite 7039 aluminum plates (50.8 mm and 76.2 mm) at nominal velocities of 2100 m/s. By using several penetrator materials (and shapes) along with multiple target thicknesses, different loading functions can be applied to the target to observe potential differences in crater formation and

debris character. Assuming that these constant energy impacts do result in distinct debris patterns, understanding the boundary conditions required to obtain a specific debris pattern and the ability to predict these patterns for more complex interactions would be beneficial. To this end, computational solid mechanics and analytic modeling techniques were employed to provide further insight into target response and debris formation.

2. Experimental setup and results

The launcher used for these experiments was a 50-mm, high-pressure powder gun capable of delivering 200-g payloads at 2100 m/s, or about 0.5 MJ impact energy. This combination of diameter, velocity, and impact energy places the projectiles under consideration in a relevant regime when considering the Army's plans for its initial technology demonstration of a 2 MJ EM gun [1].

In the initial experimental phases of the program, nylon and aluminum cylinders were used as controls for cased, reactive-material projectiles to establish experimental procedure. The purpose here was to validate velocity, confirm target thickness selections, and verify instrumentation function and experimental setup with simple, inexpensive projectiles. After obtaining interesting results from these initial experiments, a follow on set of experiments were conducted adding a steel cylinder and an aluminum cone. The steel (4340 Rc 30) projectile was added to provide a higher density and strength projectile to see if the trends in crater and spall characteristics observed for the nylon and aluminum projectiles continued. Additionally, for the 50.8-mm target, two hardnesses were used for the steel projectile to determine if different strength or elongation would change the character of the spall. The cone was added since it is aero-stable, providing

* Corresponding author. Tel.: +1 410 278 6527; fax: +1 410 278 6564.
E-mail address: sorensen@arl.army.mil (B.R. Sorensen).

Table 1
Projectile characteristics

Material	Shape	Length (mm)	Diameter (mm)	Mass (g)	L/D_{eff}
Nylon	Cylinder	101.8	50.7	236	2.00
6061 Al	Cylinder	51.6	43.6	217	1.18
4340 Steel	Cylinder	17.5	43.6	205	0.40
6061 Al	Cone	132.6	43.7	215	4.84

a quasi-tactical shape, and has a higher effective aspect ratio, leading to a penetration event rather than a shear-dominated failure mechanism in the target. The projectile configurations are presented in Table 1.

Instrumentation for these experiments included the standard striking and residual radiographs with a behind-armor-debris (BAD) collection pack. To simulate a control volume and also to completely contain the debris entering this volume, an impact chamber was constructed to simulate an interior volume behind the target. The steel impact chamber was nominally 1.37 m (4.5 ft) on a side with an interior volume of approximately 2.8 m^3 ($\sim 100 \text{ ft}^3$) which permitted a $1.2 \times 1.2\text{-m}$ ($4 \times 4 \text{ ft}$) BAD pack to be placed in the back of the impact chamber with a residual X-ray cassette for the vertical plane along right side wall. A Lexan instrumentation window was placed in the left side wall to reduce X-ray absorption and to permit high-speed photography of the debris field. Finally, orthogonal striking X-rays were used to determine impact conditions.

Experimental data are presented in Table 2. For hole, exit crater and spall-ring diameters, horizontal and vertical measurements were averaged and are illustrated in Fig. 1. Hole diameter (dashed white circle) and exit crater diameter (black dash-dot circle) have been defined to compare simulation data. Spall-ring diameter (black solid circle) refers to the lateral size of the fully developed spall ring on the back of the target. This definition was selected to provide consistency when comparing results. The large area represented by the shallow spall region, i.e. “scabbing”, did not always form and was rarely symmetric and would skew results in later analyses. Even though the crater size measurements do not encompass the entire spall ring, these details are recovered in target mass removed and the analysis of fragment size distributions.

Fig. 2 presents the normalized results for target mass removed, hole diameter and spall-ring diameter. Since the results from nylon

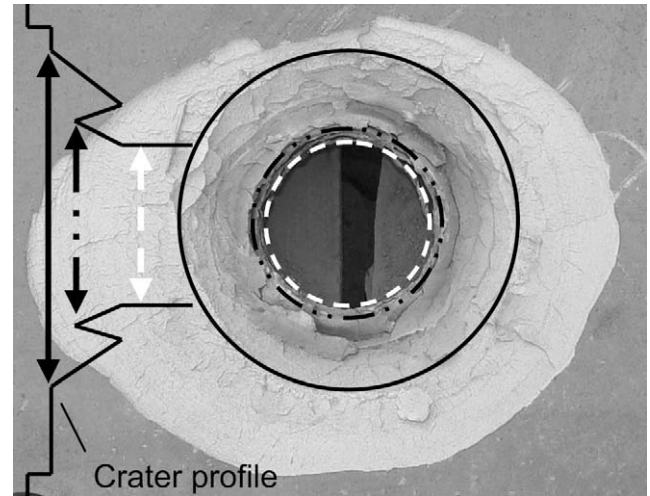


Fig. 1. Illustration of hole diameter (broken white circle), crater diameter (broken black circle), and spall-ring diameter (solid black circle) measurements. Horizontal and vertical measurements are averaged for the reported value in Table 2.

projectiles were not intended to be used in the study, impact energy and projectile diameter were not controlled, thus requiring normalization to be comparable. To normalize for energy, target mass removed was divided by impact energy and all hole/crater diameters divided by the cubed-root of impact energy for each impact. Also, since the nylon projectile had a 16% greater diameter, its results were further corrected by multiplying target mass removed by the ratio of projectile diameters squared and hole/crater diameters by the ratio of projectile diameters from Table 1. This created results with an unusual mix of units, thus, the aluminum cylinder versus the 50.8-mm plate was used as a reference baseline. For each impact, target mass removed was divided by target mass removed for the aluminum versus 50.8-mm plate result and hole diameter and spall-ring diameter were divided by the hole diameter from the baseline result, creating a set of dimensionless results to compare.

The results in Fig. 2 show that the nylon, aluminum, and steel projectiles have nearly the same craters for the 50.8-mm target with the following exceptions: the steel-30 projectile removes 9% more mass and both steel projectiles have 10–15% smaller hole

Table 2
Experimental results

Test No.	Projectile type	Striking velocity (m/s)	Total yaw (°)	Impact energy (MJ)	Residual velocity (m/s)	Target mass loss (kg)	Hole diameter (mm)	Exit crater diameter (mm)	Spall-ring diameter (mm)
<i>50.4 mm target</i>									
2497	Nylon	2206	6.4	0.57	661	1.99	103.0	116.0	149.0
2498	Nylon	2261	3.9	0.60	815	1.99	104.5	116.5	156.5
2495	Alum	2145	ND	0.50	1250 ^a	1.61	87.0	94.0	156.5
2815	Alum	2137	1.44	0.48	1011	1.81	98.0	106.5	147.5
2813	Steel-30	2135	1.38	0.47	1179	1.81	79.5	91.0	138.5
2818	Steel-30	2144	3.47	0.47	1178	1.90	76.0	88.0	141.0
2820	Steel-45	2146	1.72	0.47	1182	1.63	79.0	91.0	140.0
2821	Steel-45	2143	3.75	0.47	1154	1.63	81.5	97.5	145.5
2809	Al cone	2129	2.15	0.49	1736 ^a	0.45	42.0	52.5	84.5
2810	Al cone	2103	1.9	0.48	1821	0.45	38.5	54.0	86.5
2819	Al cone	2100	0.76	0.47	1821	0.36	39.0	58.0	78.0
<i>76.2 mm target</i>									
2496	Alum	2144	ND	0.50	592	3.17	82.1	117.5	163.5
2816	Alum	2113	1.51	0.47	606	3.08	78.5	83.0	184.0
2814	Steel-30	2085	6.26	0.45	585	3.54	87.0	100.5	174.0
2817	Steel-30	2132	2.3	0.46	711	3.54	76.5	99.0	174.0
2811	Al cone	2119	1.24	0.48	1600 ^a	0.99	39.5	61.5	119.0
2812	Al cone	2098	1.86	0.47	1499	0.99	40.0	69.5	139.5

^a Residual X-rays lost, velocities estimated from video, $\pm 80 \text{ m/s}$ error.

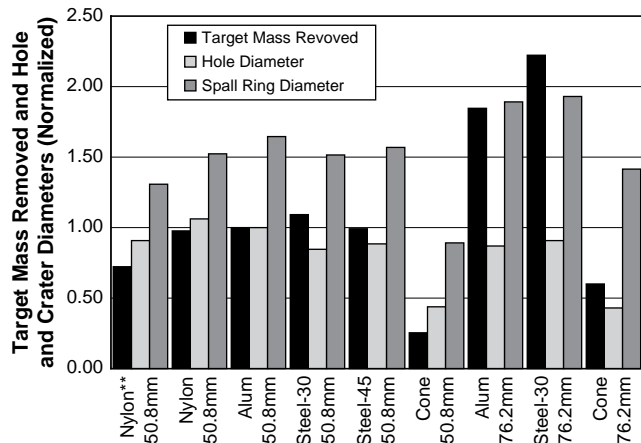


Fig. 2. Normalized target mass removed, crater diameters, and spall-ring diameters. The Nylon**–50.8-mm case has been normalized for both energy and diameter.

diameters. However, when normalizing the nylon results for diameter as well as energy, Nylon** removes 25% less mass than the aluminum baseline, generates about the same hole as the steel penetrators, but with a smaller spall ring. For the aluminum and steel projectiles striking the 76.2-mm target, the amount of material removed increases by much more than 50%, while hole diameter actually decreases from the 50.8-mm baseline and spall-ring diameter only increases slightly. This discrepancy between crater volume and diameters is resolved in Fig. 3 where representative images of the exit craters are displayed for the nylon, aluminum, steel, and conical projectiles striking both targets and it is clear that a much larger region of the target is failing in the 76.2-mm target which is not accounted for in the spall-ring diameter measurements discussed earlier. The craters resulting from the conical projectiles are much different in character and are more representative of penetration from a long rod, which is also reflected in the higher residual velocities and the fact that residual penetrators can be seen in the X-rays.

While the craters differ somewhat between the 50.8-mm and 76.2-mm targets, character of the debris is much different as illustrated by the BAD packs and fragment photographs in Fig. 3

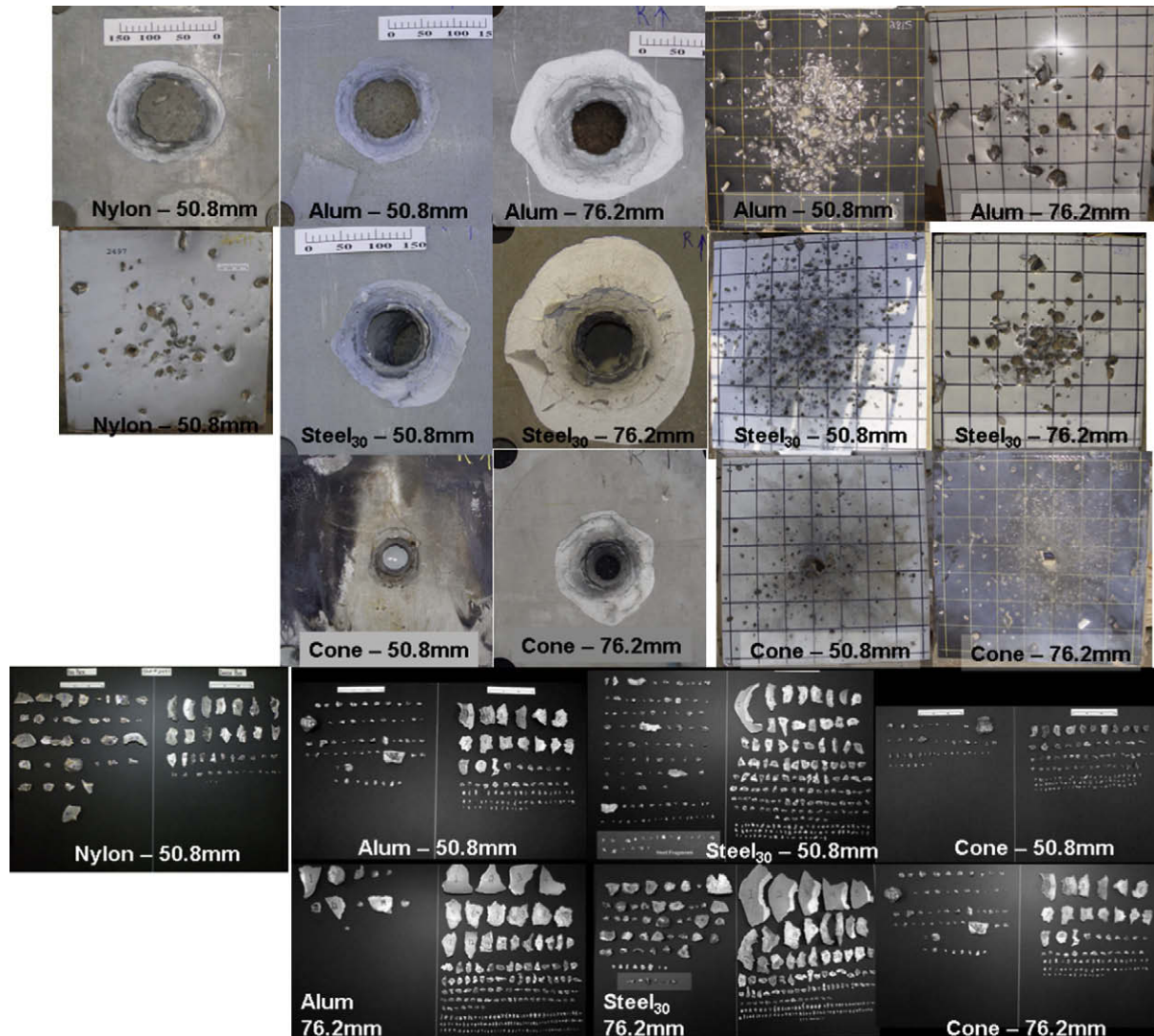


Fig. 3. Photographs of exit craters/spall rings, the 0.8-mm (1/32 in.) steel panel on the BAD pack and the corresponding fragments collected in the impact chamber for the aluminum, steel, and conical projectiles for each target thickness. Fragments on the left of each panel were recovered from the BAD pack. Fragments on the right were recovered from the floor of the impact chamber.

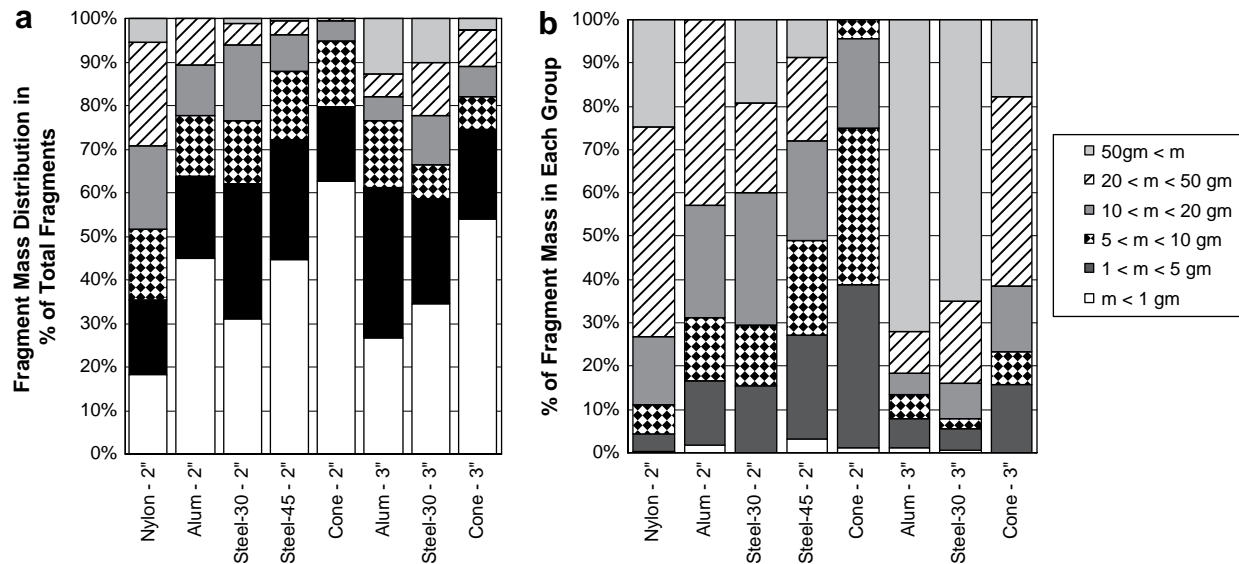


Fig. 4. Fragment mass distributions in (a) percent of total count and (b) percent of total mass for different ranges of mass for fragments recovered inside the impact chamber.

where the aluminum and steel projectiles provide much larger, but slower, fragments in the 76.2-mm target. Some of these are large “flakes” originating from the outer spall ring, but many are also from the center of the crater as seen by their location near the shot line on the BAD packs. This indicates that plastic work done during crater formation differs between the 50.8-mm and 76.2-mm targets.

Fig. 4 addresses size distribution in terms of fragment count and percent of total mass after sorting fragments into six arbitrary bins. Other than the bulk of the debris mass falling in the >50 -g range for the 76.2-mm target for the aluminum and steel projectiles and the cones yielding smaller fragments than the cylinders, little can be seen from the fragment statistics to explain the differences in the BAD packs for the cylinder impacts.

3. Numerical simulations

Three-dimensional numerical simulations of the aluminum and steel cylindrical projectiles have been conducted. The numerical study was conducted using the Eulerian wave propagation code CTH [2]. An adaptive mesh refinement (AMR) capability has been added to CTH which allows the mesh topology to change during the simulation based on the evolving characteristics of the simulation.

The AMR capability in CTH was employed to define the computational mesh. The adaptive mesh refinement algorithm in CTH is blocked based where each block is a constantly zoned, logically identical mesh. Blocks are connected in a hierarchical manner with adjacent blocks guaranteed never to exceed a ratio of

2:1 in cell size. Mesh refinement and unrefinement indicators for the simulations reported herein were based on material volume fraction in order to track material interfaces. In addition, a cell pressure difference indicator was used to accurately track shock wave propagation. A maximum of four mesh refinement levels were specified resulting in a uniform cell size of 0.9 mm in regions of maximum refinement (i.e. highest mesh resolution).

The Johnson–Cook [3] viscoplastic model was used to model the elastic–plastic behavior of all metals. A Mie–Grüneisen equation-of-state was used to describe the volumetric behavior of all materials. Material failure was modeled using the Johnson–Cook damage-accumulation fracture model in conjunction with a threshold maximum tensile stress criterion. Additional simulations were conducted using the Johnson–Cook fracture model with a Weibull statistical distribution for the initial failure strain for the 7039 aluminum alloy target material only. The statistical fracture model provides a spatially random distribution of values for the initial failure strain, although in the aggregate its population is Weibull-distributed. This model permits non-uniform, stochastic failure of the aluminum plate. The non-uniformity of material failure is strongly dependent on the nature of the Weibull distribution for the initial failure strain, as quantified by the Weibull modulus, jfw , which is a user-specified input to CTH. The effects of the Weibull modulus on the predicted behind-armor-debris characteristics were examined in this study for Weibull modulus (jfw) values of 4, 8, and 12.

The CTH predicted behind-armor-debris fields for the aluminum projectile impacting the 50.8-mm aluminum alloy target plate at

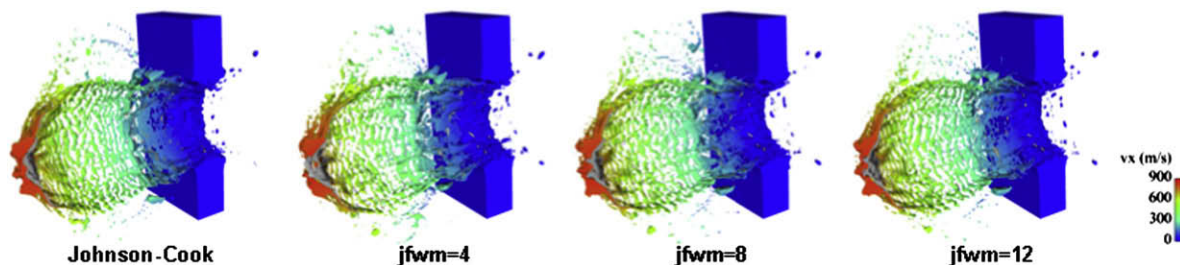


Fig. 5. CTH behind-armor-debris fields for uniform (Johnson–Cook) and Weibull distributions of initial failure strain for aluminum projectile impact on 50.8-mm aluminum target, $t = 350 \mu s$.

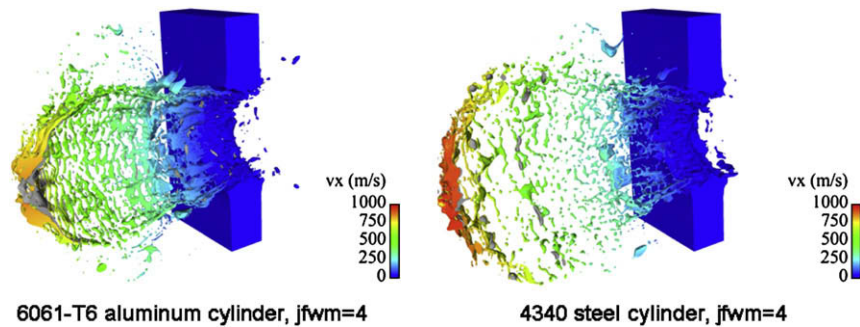


Fig. 6. CTH behind-armor-debris fields for steel and aluminum projectiles impacting 50.8-mm aluminum target, $t = 350 \mu\text{s}$.

2.2 km/s for uniform (i.e. Johnson–Cook) and Weibull distributions of the initial failure strain are shown in Fig. 5. The debris field is colored by the magnitude of the axial component of the velocity vector at $350 \mu\text{s}$ and the residual penetrator material is shaded gray. The predicted debris fields are nearly identical. The Weibull-distribution debris fields have an average maximum axial velocity of 874 m/s. The uniform distribution predicts a lower value of 859 m/s. The predicted debris fields can be characterized as being comprised of a large number of small fragments.

A comparison of the predicted debris fields for a Weibull modulus value of 4 for both the steel and aluminum projectiles is shown in Fig. 6. Some differences in the debris fields are noted. The debris field from the steel projectile has a larger radial expansion and has expanded further down range at $350 \mu\text{s}$. The maximum axial component of the velocity vector for the steel projectile is 980 m/s as compared to 876 m/s for the aluminum projectile. Both projectiles produce a debris field comprised of small fragments.

The CTH predicted behind-armor-debris fields for the aluminum projectile impacting the 76.2-mm aluminum alloy target plate at 2.1 km/s for uniform (i.e. Johnson–Cook) and Weibull distributions of the initial failure strain are shown in Fig. 7. The debris field is colored by the magnitude of the axial component of the velocity vector at $700 \mu\text{s}$ and the residual penetrator material is shaded gray. Distinct differences in the character of the debris fields are noted. The uniform distribution shows a low-velocity annular ring of target material being ejected from the target. While each of the Weibull distributions show a fragmented annular ring of target material, their debris fields are very similar in overall characteristics. In contrast to the debris fields predicted for the 50.8-mm target, the debris predicted for the 76.2-mm target is comprised of low-velocity chunky fragments. The average maximum axial velocity for the uniform and Weibull distributions is 382 m/s, so the 2.1 km/s impact velocity is approaching the limit velocity for the 76.2-mm target.

Contours of Johnson–Cook damage accumulation for the 76.2-mm target plate, for a Weibull modulus value of 4, are presented in Fig. 8. Note the presence of highly localized fingers of fully damaged (damage value of 1) target material which suggests a shear-

dominated failure mechanism. The damage contours observed at $700 \mu\text{s}$ suggest that additional target material may be ejected from the crater walls after $700 \mu\text{s}$.

The predicted debris fields for a Weibull modulus value of 4 for both the steel and aluminum projectiles are shown in Fig. 9. Some differences in the debris fields can be observed. Fragments generated by impact of the aluminum projectile are larger and the maximum axial velocity of the debris field is 394 m/s. In contrast, the fragments generated by the steel projectile impact are smaller, but the maximum axial velocity (498 m/s) is higher.

4. Analytical modeling

While the CTH results show great promise in predicting the size of the residual fragments, it is highly desirable to generate an estimate of this debris field with a quick analytical algorithm. Here, we have used the Walker–Anderson penetration model [4] along with the exit modes from the Ravid–Bodner [5] penetration analysis (as described in Chocron et al. [6]) to examine this debris field.

The Walker–Anderson model requires a small number of material constants. Here, we concentrate on the aluminums (7039 and 6061-T6). The density of both materials is taken to be 2.7 g/cm^3 , with the Young's moduli and shear moduli taken to be 69 GPa and 26 GPa, respectively. The equation-of-state is represented by a linear U_s-U_p relation, with the bulk sound speed taken to be $c_0 = 5.386 \text{ km/s}$ and the slope taken to be $s_1 = 1.339$ for both materials. The only major difference in the materials is the strength (yield). Here, we take the quasi-static yield as the strength of the penetrator and target.

The only other properties/relations needed by the model are (1) the radius of the crater and (2) the fracture strain of the target. The radius of the crater is simply taken as the radius of the hole in the target in the experiment. The fracture strain is difficult to deduce at these rates without experimental data; here, it is treated as a variable and is varied to see its effect on the debris field. Simulating shots 2815 and 2816 (6061-T6 cylindrical projectiles at nominally 2100 m/s into 50.8-mm and 76.2-mm thick 7039 targets), one sees the residual velocity as a function of the failure strain in Fig. 10. A

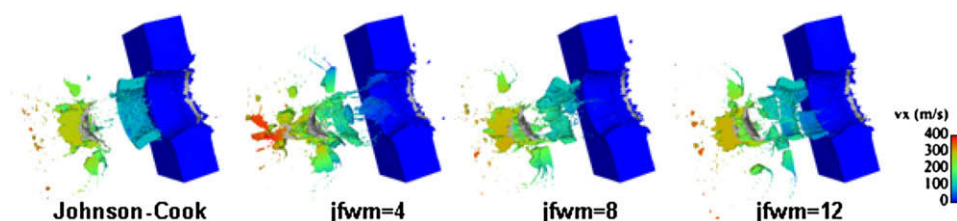


Fig. 7. CTH behind-armor-debris fields for uniform (Johnson–Cook) and Weibull distributions of initial failure strain for aluminum projectile impact on 76.2-mm aluminum target, $t = 700 \mu\text{s}$.

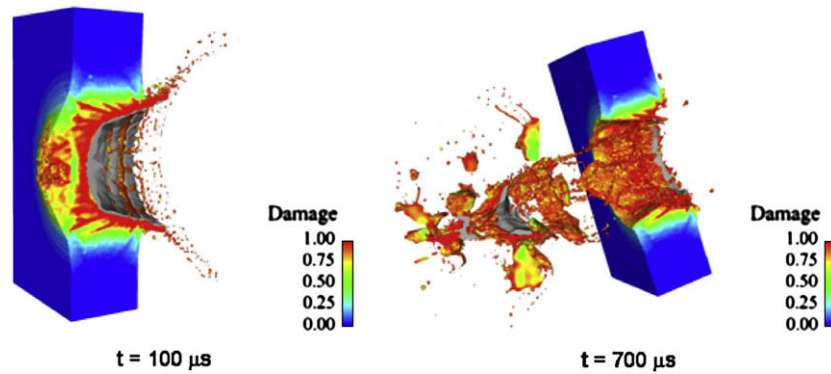


Fig. 8. Contours of Johnson–Cook damage accumulation for aluminum projectile impact 76.2-mm aluminum target at 2.1 km/s (Weibull modulus value of 4).

failure strain of 0.1 overpredicts the residual velocity for the 50.8-mm target by 9.5% while it underpredicts the residual velocity for the 76.2-mm target by 15%. Considering that the Walker–Anderson model is derived for long rod ($L/D \ll 1$) penetrators, these results are reasonable (for an $L/D \sim 1$ penetrator).

Using the analytical solution in Chocron et al. [6] one can use a Grady–Kipp [7] analysis to estimate the fragment distribution (as described in Refs. [6] and [7]). Here, the effective strain rate is calculated as a function of distance ahead of the penetrator, and is used to make an estimate of fragment sizes, based on the published range of the fracture toughness $K_f = 15\text{--}35 \text{ MPa m}^{1/2}$ for 7075 aluminum [6]. Fig. 11 shows the fragment sizes created for the two different target thicknesses for three values of fracture toughness. The point represents the mean fragment size, while the error bars encompass the span of fragment sizes.

Note that lower fracture toughness results in a much smaller spread in the fragment sizes and the higher residual velocity due to the thinner target plate (and thus higher strain rates) results in smaller fragments.

5. Discussion

Before contrasting the computation and analytic results with the experimental results, a brief discussion on whether the results agree intuitively with expectations will be provided. First, due simply to projectile/target geometry, a larger spall surface should be seen in the 76.2-mm target since the spherical shock wave can expand to a larger lateral area before the magnitude of the reflected wave falls below the spall threshold. Second, as the limit velocity, or thickness in this case, is approached, strain rate within the crater as the rear surface of the target is approached should be lower, leading to larger fragments. This is evident as the residual velocity

decreases from 53% of impact velocity to 28% as target thickness increases and larger fragments are clearly present in the BAD packs as displayed in Fig. 2 for the thicker targets. Furthermore, while the fully developed spall ring does not increase significantly with target thickness, the spalled area of the target increases significantly for the thicker target.

In general, CTH follows the same trends as the experiments; bigger, slower fragments with increasing target thickness. Specifically, for the aluminum and steel projectiles versus the 50.8-mm target for residual velocity, hole diameter and spall-ring diameter, CTH differs from the experiments by -15% , $+10\%$ and -18% , respectively. For the 76.2-mm target, the comparisons were -30% for velocity and -30% for spall-ring diameter and hole diameters for the aluminum and steel projectiles were $+40\%$ and $+7\%$, respectively; a much larger and unexplained difference than all other values. Underpredicting residual velocity is not unexpected due to weaknesses in the failure models. If shear banding or fracture capabilities had been included, target failure may have occurred at an earlier time, leading to higher residual velocities.

Comparing crater profiles is more difficult due to the temporal nature of damage evolution in the target. Since high-speed photography was used to observe the debris cloud, additional insight can be gained far beyond the normal residual X-ray “snapshots” and BAD impacts as illustrated in Fig. 12. Here, three frames have been provided to show three different target failure modes. The first two images show the typical ellipsoidal debris cloud forming of material from the penetration crater. In the second image, the circled area shows the initial material from the spall ring. In the third image, the three arrows show additional material originating from inside the crater in the manner indicated earlier in Fig. 8. Tracing these fragments back to the target shows that the spall ring is separating at $100\text{--}300 \mu\text{s}$ after target failure and the

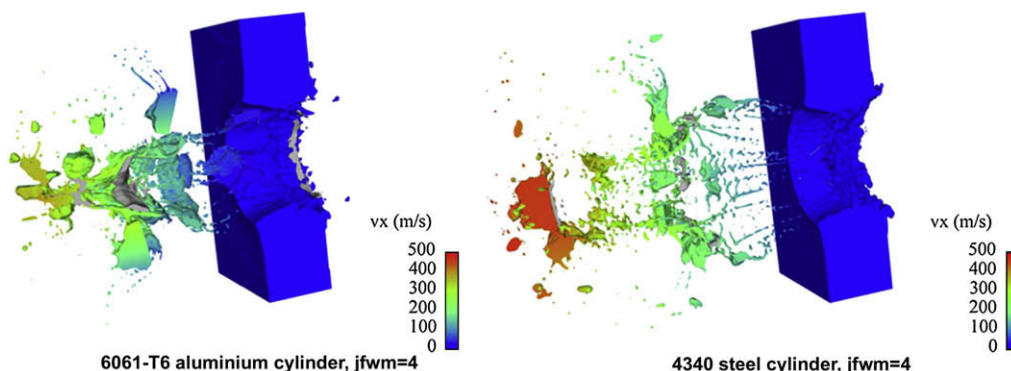


Fig. 9. CTH behind-armor-debris fields for steel and aluminum projectiles impacting 76.2-mm aluminum target, $t = 700 \mu\text{s}$.

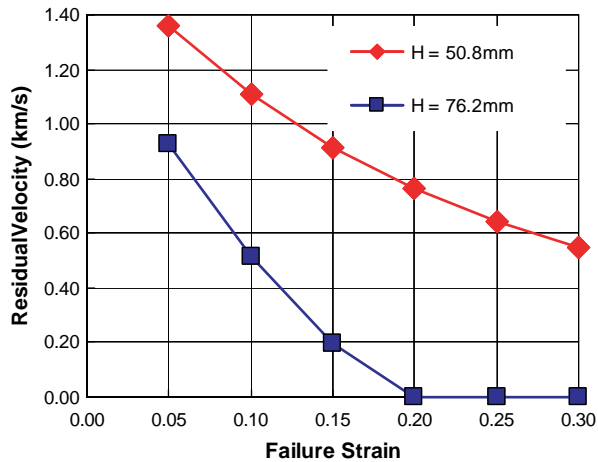


Fig. 10. Residual velocity as a function of failure strain for 6061-T6/7039 impacts of different target thicknesses.

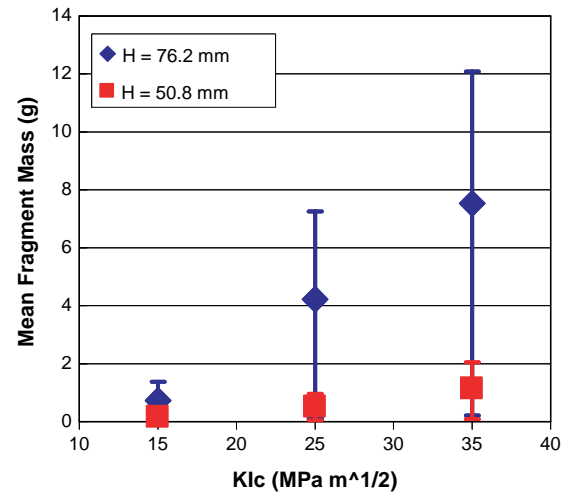


Fig. 11. Fragment size as a function of fracture toughness for the Grady-Kipp analysis.

spall from inside the crater is forming 1400 μ s after target failure, significantly beyond the times of the simulations. This late-time damage helps to explain why CTH can overpredict hole diameter and underpredict the spall-ring diameter since the simulation is halted well before the failures occur.

Similar logic can be applied to analytic model's fragment distributions and whether only fragments originating from the impact crater and not the spall rings should be considered. Using all of the fragment data, the median fragment mass was 2 g for both targets and the average fragment masses were 6.5 and 14.5 for the 50.8-mm and 76.2-mm targets, respectively. However, if the five biggest fragments were removed for each target, average masses decreased to 5.5 g and 8.7 g, giving much better agreement with the predictions of 1.5 g and 8.0 g. The analytical model, while

reasonably capturing the trend of the impact crater fragment sizes, is not capable of capturing the spall and late-time behavior seen in the experiments; its usefulness is limited as such.

To summarize, the trends observed in the simulations and analytic models are consistent with intuition and also agree well with experimental results. However, the evolution of the large spall-ring fragments occurred a much later time than anticipated; further work will help determine if hydrocode models can accurately predict the creation of these fragments.

6. Conclusions

This paper presented a series of experiments of nylon, aluminum, and steel projectiles striking aluminum armor at 2100 m/s to

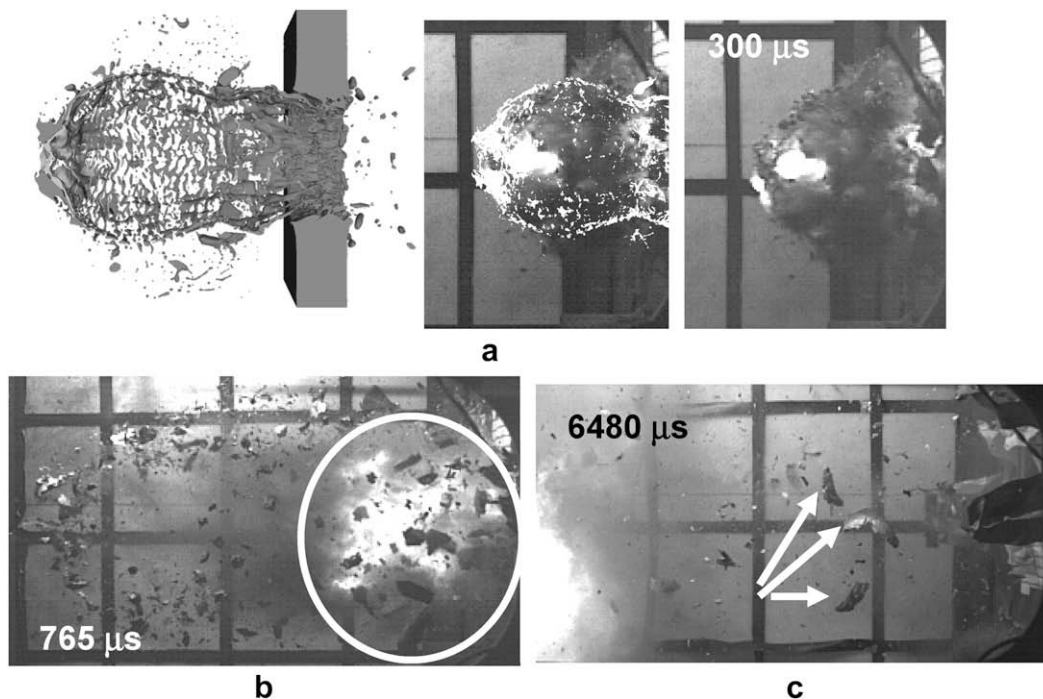


Fig. 12. Debris clouds for the aluminum projectile striking the 50.8-mm target. For the experiments, times are relative to target failure. In (a), the center image is a superposition of the CTH simulation on the left and the experiment on the right at equivalent times. In (b) and (c), late-time images illustrating spall formation in (b) and additional crater growth in (c).

examine defeat mechanisms different than classical high-density penetrators. Projectile aspect ratios were very low and projectile diameters were similar to target thickness. The experiments demonstrated that depending on the level of ballistic over match, different fragment mass and spatial distributions could be obtained. The constant diameter, mass, and energy projectiles of aluminum and steel created nearly identical results, indicating for the conditions examined, there was not a material preference. However, it was clear that for the different levels of overmatch, the changes in the debris would have a dramatic affect on damage capacity behind the target. To further understand the mechanics occurring in the target, simulations and analytic modeling were performed, and in general, agreement with the experiments was very good. Both matched the experimental trends in predicting residual velocity and fragment sizes. However, only the small portion of the debris mass originating from the crater was well characterized by the analytic method, debris from the spall rings was substantially larger and possibly more lethal. While the simulations capture this trend, carrying the

simulations forward to predict damage capacity is time intensive, thus additional analytic models to predict the debris character of material originating from the spall ring may be required.

References

- [1] Cilli M. US army program overview. In: 13th electromagnetic launcher symposium, Potsdam, Germany; 22–25 May 2006.
- [2] McGlaun JM, Thompson SL. CTH: a three-dimensional shock wave physics code. *Int J Impact Eng* 1990;10(1–4):351–60.
- [3] Johnson GR, Cook WH. A constitutive model and data for metals subjected to large strains, high strain rates and high temperatures. In: Proceedings of the seventh international symposium on ballistics. The Hague, Netherlands: Royal Institution of Engineers in the Netherlands (Kivl); 19–21 April 1983. p. 541–7.
- [4] Walker JD, Anderson CE. A time-dependent model for long-rod penetration. *Int J Impact Eng* 1995;16:19–48.
- [5] Ravid M, Bodner SR, Holzman I. Analysis of very high speed impact. *Int J Eng Sci* 1987;25(4):473–82.
- [6] Chocron S, Anderson CE, Walker JD, Ravid M. A unified model for long-rod penetration in multiple metallic plates. *Int J Impact Eng* 2003;28:391–411.
- [7] Grady DE, Kipp ME. Fragmentation properties of metals. *Int J Impact Eng* 1997;20:293–308.

NO. OF
COPIES ORGANIZATION

1 DEFENSE TECHNICAL
(PDF INFORMATION CTR
only) DTIC OCA
8725 JOHN J KINGMAN RD
STE 0944
FORT BELVOIR VA 22060-6218

1 DIRECTOR
US ARMY RESEARCH LAB
IMNE ALC HRR
2800 POWDER MILL RD
ADELPHI MD 20783-1197

1 DIRECTOR
US ARMY RESEARCH LAB
RDRL CIM L
2800 POWDER MILL RD
ADELPHI MD 20783-1197

1 DIRECTOR
US ARMY RESEARCH LAB
RDRL CIM P
2800 POWDER MILL RD
ADELPHI MD 20783-1197

ABERDEEN PROVING GROUND

1 DIR USARL
RDRL CIM G (BLDG 4600)

INTENTIONALLY LEFT BLANK.